J. Fluid Mech. (1991), *vol.* 227, *pp.* 509–525
Printed in Great Britain

Turbulent Couette flow profiles that maximize the efficiency function

By L. M. SMITH†
Massachusetts Institute of Technology, Department of Mathematics,
Cambridge, MA 02139, USA

(Received 17 April 1989 and in revised form 3 December 1990)

A previous study revealed that only maximization of the efficiency function, from among a large class of mean field moments, results in both a logarithmic law and a velocity defect law in turbulent Poiseuille channel flow. The efficiency function, $\mathscr{E}$, is the product of a drag coefficient and the ratio of the fluctuation and mean dissipation rate integrals. Here, maximum $\mathscr{E}$ is explored in Couette flow to test its generality as a statistical stability criterion for turbulent shear flows. The optimal flow exhibits a logarithmic law but does not have a velocity defect law. A decreasing velocity defect is predicted for Reynolds numbers up to 30000. This prediction is shown to be supported by the existing data, which are limited to Reynolds numbers less than 20000.

1. Introduction

A recent study established that maximum 'efficiency' leads to the observed scaling laws in the mean velocity of turbulent Poiseuille flow, whereas 'nearby' moments do not scale like the data (Malkus & Smith 1989, hereinafter referred to as I). The efficiency function is defined as

$$\mathscr{E} \equiv C_D I,$$

where C_D is a drag coefficient and I is the ratio of the flow-averaged fluctuation dissipation rate and the flow-averaged mean dissipation rate. The present study explores maximum efficiency in turbulent Couette flow.

This work is a further step towards the goal of establishing a statistical stability criterion for turbulent shear flows. The approach taken is based on ideas introduced by Malkus (1954, 1956), and will be referred to as 'optimal theory'. In optimal theory, the selection of a turbulent flow field is achieved by optimization of a flow quantity subject to constraints derived from the Navier–Stokes equations. Such an optimization problem provides a complete, mechanistic idealization of the flow, whose statistical properties can be compared with experimental observations and direct numerical simulations.

The constraints of the optimization problem define a vector space which includes the solutions of the Navier–Stokes equations. The vector space is reduced with the addition of more constraints. If enough constraints are incorporated, the space of admissible vectors will be almost as small as the space defined by the Navier–Stokes equations. In that case, optimization of any function will result in a 'flow' with characteristics of realized turbulence. With a large number of constraints, however,

† Currently at The Center For Turbulence Research, Building 500, Stanford University, Stanford, CA 94305-3030, USA.

the optimization problem becomes almost as difficult as solving the Navier–Stokes equations. A useful optimal theory isolates a flow quantity that reflects the essential physics with only a few constraints.

The solutions of optimization problems are ordered and smooth. This may seem incompatible with the intermittency in turbulence and the more conventional closure theories that model small-scale disorder. However, the proposal is not that optimal theory can be a final picture of turbulence. Rather, we seek a satisfying first description in terms of a physical principle. The optimal flow will hopefully capture ordered features of turbulent flows, such as the streaks observed in experiments and numerical calculations of wall-bounded shear flows.

Subsequent to the introduction of optimal theory, reviews by Howard (1972), and later Busse (1978), emphasized the mathematical problem of bounding flow quantities. They developed techniques to bound the transport of heat, mass or momentum in turbulent flows.

In the context of turbulent convection, Busse (1969*b*) found a multiple boundary-layer solution for the fluctuating field of maximum heat transport. The multiple boundary-layer solution is a consequence of continuity and the two dissipation rate integrals of the Boussinesq equations. Its structure of nested rolls provided insight into the physical mechanism responsible for efficient heat transport. Eddies of larger and larger scale continue the transfer of heat away from the boundary.

Busse then considered the maximum transport solutions of wall-bounded shear flows (Busse 1970). He showed that the continuity condition and the dissipation rate integral of the Navier–Stokes equations also lead to a structure of nested rolls. The axis of the rolls is in the downstream direction. At any given Reynolds number, the smallest roll defines the size of the viscous boundary layer. An upper bound on transport is associated with a lower bound on the size of the boundary layer.

The upper bounds on mass and momentum transport, subject only to the constriants of continuity and the dissipation rate integral, are much higher than the realized values. For example, the multi-wavenumber, optimal field for pipe flow yields a drag coefficient which is 20 times that observed at a Reynolds number of 10^7. The difference is increasing with Reynolds number.

The maximum transport fields do not exhibit observed scaling laws. There are two reasons why the maximum transport fields bear little resemblance to turbulent shear flows. First, shear turbulence apparently does not tend to maximize transport. Second, the optimal flows are insufficiently constrained. For an optimal flow to approach the realized flow, the bounding quantity must adequately approximate nature's way of choosing between solutions. The constraints must capture the local physics of (solutions to) the equations of motion.

Here we return to the search for a criterion governing shear flow stability, and to the isolation of a flow quantity that exhibits observed scaling laws with only a few simple constraints. As stability is meant in the statistical sense, the optimal problem is formulated in terms of mean quantities (see I). For Poiseuille flow, only the mean velocity associated with maximum $\mathscr{E}$ exhibits both a logarithmic law and a velocity defect law. Apparently, the important global dynamics of turbulent Poiseuille flow are represented in the efficiency function.

Section 2 of this paper reviews the optimization problem for the mean. The specifics of its application to Couette flow are given in §3. Section 4 describes in detail the maximum-$\mathscr{E}$ solution. A qualitative and quantitative comparison with experimental observations is made in §5. Implications and future work are discussed in §6.

2. A problem for the mean flow

2.1. *The optimization scheme*

Our investigation is of statistically steady, parallel shear flows, homogeneous in the horizontal directions. For these flows, the primary goal is to predict variation in the vertical direction. The mean flow is thus defined as the average in the x-, y- and t-directions. A formal problem for the mean, introduced in I, is the optimization of a mean field moment subject to:

(i) boundary conditions for the mean;

(ii) the existence of a viscous boundary layer whose scale is a lower bound on the observed scale;

(iii) the inviscid, linear stability condition at all larger scales.

The optimization principle selects a profile from among those defined by constraints (i)–(iii).

The emphasis of this study is on qualitative agreement with the data. Qualitative agreement (or disagreement) between the deduced and realized mean flows depends primarily on the choice of moment. The main question addressed is 'Does the mean velocity deduced for maximum $\mathscr{E}$ have the structural features and scaling observed in turbulent Couette flow, while adjacent moments fail to scale like the data?' The quantitative features of the optimal flow are controlled by the size of the boundary layer. Section 4.3 shows how quantitative agreement can be approached.

The separation of the qualitative and quantitative features of optimal flows is clearly demonstrated by the study of Poiseuille flow in I. The optimal mean velocity profiles for a variety of mean field moments were found, keeping the constraints fixed. All of the optimal flows are an order of magnitude too large because the bound on the viscous boundary-layer scale is an order of magnitude too low. The mean of maximum $\mathscr{E}$ agrees qualitatively with the data, despite insufficient constraints. Optimization of other moments fails even at the qualitative level.

2.2. *Motivation for the constraints*

The formal upper-bound problems solved by Howard (1972) and Busse (1970) select a value for the scale of the viscous boundary layer of the maximum transport solutions. As mentioned in the Introduction, an upper bound on transport is associated with a lower bound on the realized viscous boundary-layer scale. This lower bound is a consequence of the dissipation rate integral, the only viscous constraint used in the upper-bound problems of Howard and Busse.

Here we use the Busse–Howard value of the boundary-layer scale. Comparison with Busse's maximum transport solutions are then possible. It should be emphasized that we are proposing a statistical theory based on an optimization principle, rather than a mathematically rigorous upper bound. However, by borrowing the Busse–Howard lower bound for the viscous boundary-layer scale, our maximal statistics will also bound the realized turbulent statistics from above.

All larger scales must also be constrained for the problem to be bounded. We take the view that the important interior dynamics are inviscid. The interior mean, maintained by infrequent 'bursts', is at least stable to linear disturbances. We therefore constrain the flow with Fjørtoft's condition for inviscid, linear stability (Drazin & Reid 1981). Arnol'd (1965) showed that Fjørtoft's condition also implies stability of steady, two-dimensional, inviscid flow to small finite-amplitude disturbances. Also note that Fjørtoft's condition is satisfied by Busse's maximum transport solutions. Finally, Fjørtoft's stability condition is satisfied by observed

shear turbulence, though it is not yet a proven consequence of the full Navier–Stokes equations. This ensures that the realized solution lies within the vector space defined by the constraints.

2.3. *Improving the lower bound on the viscous boundary-layer scale*

As the only viscous constraint in the upper-bound problems solved by Howard (1972) and Busse (1969*a*, 1970), the dissipation rate integral of the Navier–Stokes equations provides a poor lower bound on the viscous boundary-layer scale, and thus poor quantitative agreement with realized turbulent statistics. The dissipation rate integral is a statement of the global energy balance imposed by the Navier–Stokes equations. In retrospect, it should be no surprise that approximate equations based largely on overall energy balance are far from satisfactory. Analysis shows that the integral statement of energy balance does not capture the relevant stability mechanism at work in shear flows (Joseph 1976). Many studies have revealed the importance of vorticity to shear stability (Bayly, Orszag & Herbert 1988). A constraint reflecting vorticity balance is likely to improve the bound on the viscous boundary-layer scale and bring the quantitative aspects of optimal statistics much closer to the observations.

3. Application to Couette flow

3.1. *The basic equations*

The incompressible Navier–Stokes equations are

$$\left.\begin{aligned} \frac{\partial \boldsymbol{v}}{\partial t} + (\boldsymbol{v}\cdot\boldsymbol{\nabla})\,\boldsymbol{v} &= -\frac{1}{\rho}\boldsymbol{\nabla}P + \nu\boldsymbol{\nabla}^2\boldsymbol{v}, \\ \boldsymbol{\nabla}\cdot\boldsymbol{v} &= 0, \end{aligned}\right\} \tag{3.1}$$

where $\boldsymbol{v}$ is the velocity, P is the pressure, ρ is the density and ν is the kinematic viscosity. The downstream, spanwise and vertical directions are x, y and z, respectively. Plane Couette flow is induced by differential motion of infinite parallel plates. The plates move with equal speeds in opposite directions for convenience, $\boldsymbol{v} = \pm\boldsymbol{v}_{\text{wall}}$ on $z = \pm h$.

For statistically steady Couette flow, an average in the homogeneous directions, x, y and t, of (3.1) gives

$$\nu\frac{\mathrm{d}^2U}{\mathrm{d}z^2} = \frac{\mathrm{d}\overline{uw}}{\mathrm{d}z}, \tag{3.2}$$

where the overbar denotes the (x, y, t)-average and $\bar{\boldsymbol{v}} \equiv U(z)\,\hat{\boldsymbol{\imath}}$. The downstream and vertical components of $\boldsymbol{u} \equiv \boldsymbol{v} - \bar{\boldsymbol{v}}$ are u and w, respectively.

An expression for the mean shear is found by integration of (3.2),

$$\nu\frac{\mathrm{d}U}{\mathrm{d}z} = \overline{uw} + \tau_0, \tag{3.3}$$

where $\overline{uw}$ is the Reynolds stress and τ_0 is the stress per unit mass at the wall.

For consistency with the engineering data all velocities will be non-dimensionalized with the friction velocity, $U_\tau \equiv \tau_0^{\frac{1}{2}}$, and all lengths with the half-channel width h. The notation $\boldsymbol{v}^+ \equiv \boldsymbol{v}/U_\tau$ is used to distinguish the non-dimensional form of the velocity and from now on $-1 \leqslant z \leqslant 1$. Equation (3.3) is then written

$$\frac{\mathrm{d}U^+}{\mathrm{d}z} = R_\tau\overline{uw}^+ + R_\tau, \tag{3.4}$$

where $\overline{uw}^+ \equiv \overline{uw}/U_\tau^2$ and $R_\tau \equiv U_\tau h/\nu$ is the friction Reynolds number.

The rigid boundary conditions are $u^+ = w^+ = \mathrm{d}w^+/\mathrm{d}z = 0$ at $z = \pm 1$. The boundary conditions on $\boldsymbol{u}^+$ and (3.2) determine the boundary conditions on U^+,

$$\frac{\mathrm{d}^3U^+}{\mathrm{d}z^3} = \frac{\mathrm{d}^2U^+}{\mathrm{d}z^2} = 0, \quad \frac{\mathrm{d}U^+}{\mathrm{d}z} = R_\tau, \quad U^+ = \pm\frac{R}{R_\tau} \quad \text{at} \quad z = \pm 1, \tag{3.5}$$

where $R \equiv U_{\mathrm{wall}}h/\nu$ is the Reynolds number. Multiplication of (3.4) by $R_\tau^2\,\mathrm{d}U^+/\mathrm{d}z$, followed by integration using the boundary conditions (3.5), gives the dissipation rate equation,

$$R_\tau^2\left\langle\left(\frac{\mathrm{d}U^+}{\mathrm{d}z}\right)^2\right\rangle - R_\tau^3\left\langle\frac{\mathrm{d}U^+}{\mathrm{d}z}\overline{uw}^+\right\rangle = RR_\tau^2. \tag{3.6}$$

Here $\langle\,\rangle$ indicates an average over z. The flow-averaged mean dissipation rate is $R_\tau^2\langle(\mathrm{d}U^+/\mathrm{d}z)^2\rangle$ and the flow-averaged fluctuation dissipation rate is $-R_\tau^3\langle\overline{uw}^+\,\mathrm{d}U^+/\mathrm{d}z\rangle$. Their sum is equal to the total dissipation rate, RR_τ^2.

3.2. *The wavenumber expansion*

Fourier analysis of the Howard–Busse optimal mean flows provides an abrupt cutoff wavenumber, motivating the use of a finite series expansion for the mean (Busse 1969*a*). The cutoff wavenumber will be estimated from above in the following to preserve the upper bound character of the analysis. In real flows, one expects exponential decay of the expansion coefficients for wavenumbers beyond the cutoff.

Most series expansions are inconvenient for this problem because Fjørtoft's stability condition is local, and must be satisfied at every point in the flow. For most series, for example Fourier or Chebyshev, this implies a number of constraints equal to the highest wavenumber. This difficulty is avoided if the expansion is chosen to automatically satisfy Fjørtoft's condition (Malkus 1979).

Fjørtoft's condition for inviscid, linear stability is

$$\frac{\mathrm{d}^2U^+}{\mathrm{d}z^2}(U^+ - U_{\mathrm{s}}^+) \geqslant 0 \quad (-1 \leqslant z \leqslant 1), \tag{3.7}$$

where $U_{\mathrm{s}}^+ \equiv U^+(z_{\mathrm{s}})$ and $\mathrm{d}^2U_{\mathrm{s}}^+/\mathrm{d}z^2 = 0$. Fjørtoft's condition and antisymmetry imply that U^+ and $\mathrm{d}^2U^+/\mathrm{d}z^2$ change sign only at $z = 0$. A convenient representation of the mean is therefore

$$\frac{\mathrm{d}^2U^+}{\mathrm{d}z^2} = f(\pi z)\,I{*}I \quad (-1 \leqslant z \leqslant 1), \tag{3.8}$$

together with the restriction

$$\frac{\mathrm{d}U^+}{\mathrm{d}z} \geqslant 0 \quad \text{at} \quad z = 0, \tag{3.9}$$

where the function f is antisymmetric about $z = 0$ and negative in $-1 \leqslant z \leqslant 0$. In addition, f must have a wavelength of at least 2π so that U^+ changes sign only at $z = 0$. Inflexions of the wrong sign are excluded by the restriction on the slope at $z = 0$, relation (3.9). To preserve the truncation one must also require that f is expressible as a finite Fourier sine series.

The series I is defined by

$$I \equiv \sum_{k=0}^{k_0} I_k\,\mathrm{e}^{\mathrm{i}k\phi}, \tag{3.10}$$

where $\phi/\pi = z+1$, the I_k are amplitudes and $k = 0, 1, 2, \ldots, k_0$ is the wavenumber. The double series I^*I is called a Fejér series. Fejér showed that I^*I is a complete representation of an everywhere-positive definite function when $k_0 \to \infty$.

By completeness, the results of any maximization problem should be independent of f for large k_0 except near $\phi = \pi$ ($z = 0$). The rate at which U^+ approaches zero at $\phi = \pi$ is fixed by f. The choice $f = \sin(\phi - \pi)$ forces $U^+ \sim c_1(\phi-\pi) + c_2(\phi-\pi)^3$ for $\phi \sim \pi$, where c_1 and c_2 are constants; $f = \sin(\phi-\pi)$ allows for a finite slope through the centre.

To summarize, the boundary conditions for the mean are given by (3.5); both the existence of a boundary layer and linear inviscid stability are guaranteed by (3.8)–(3.10). In §3.3, the boundary-layer scale is expressed in terms of the highest Fejér wavenumber. In §3.4, the boundary conditions are used to derive three relations among the I_k, which are constraints on the optimization problem in Fejér space.

3.3. *The boundary-layer scale*

The goal of this section is to establish a relation between the stress, R_τ^2, and the highest wavenumber of the fluctuations, k_0. With anticipation that this relation can be found with an appropriate stability problem, we define a stability parameter for the viscous boundary layer, $R_c = R_c(R_\tau, k_0)$.

In the laminar sublayer, the Reynolds stress is small and the mean is approximately linear. Near the lower boundary $\phi = 0$, using boundary conditions (3.5),

$$U^+ - \frac{R}{R_\tau} = R_\tau \frac{\phi}{\pi} + O(\phi^4) = z^+ + O((z^+)^4), \tag{3.11}$$

where z^+ is the traditional boundary-layer variable, $z^+ \equiv R_\tau \phi/\pi$. The interval in which the linear approximation to (3.11) is valid defines the lengthscale of the laminar sublayer, $z_c^+ \nu/U_\tau$. The Reynolds number of the sublayer, based on the velocity difference across the interval and the full width, is given in wall units as

$$R_c \equiv (z_c^+)^2. \tag{3.12}$$

The Reynolds number R_c has the critical value corresponding to marginal, finite-amplitude stability of the boundary layer.

As in I, we take $z_c^+ = 4R_\tau/k_0$ corresponding to twice the Fejér wavelength $\phi = 2/k_0$. Thus (3.12) becomes

$$R_c = 4R_\tau^2 \left(\frac{2}{k_0}\right)^2. \tag{3.13}$$

Using (3.13), one may estimate R_c from the maximum transport theories of Howard and Busse. The height of Busse's smallest roll is $z^+ = 3.15$ (Busse 1970). Taking the height of the smallest roll to be one Fourier wavelength of the fluctuating field in the vertical direction gives $3.15 = R_\tau 2/k_0$, which in turn leads to $R_c = 4(3.15)^2 = 39.69$. Since $z^+ = 3.15$ is a conservative lower bound on the realized height of the boundary layer, $R_c = 39.69$ is a significant underestimate of the realized R_c. In the present formulation, R_c should be regarded as a bound from below on the boundary-layer thickness.

The profiles found using (3.13) are consistent, indicating that $z_c^+ = 4R_\tau/k_0$ is a good estimate of the sublayer height in terms of the Fejér wavelength. For example, for $R_c = 39.69$, the end of the boundary layer is at roughly $z_c^+ = 2 \times 3.15 = 6.3$ (figure 2).

With k_0 related to R_c (fixed) and R_τ by (3.13), the two parameters characterizing the flow are as usual. They are the Reynolds number, R, and the stress, R_τ^2 (non-

dimensionalized). Only one of the two is free. One can maximize $\mathscr{E}$ as a function of R_τ, for fixed R, or as a function of R, for fixed R_τ. The former problem is presented here. The latter problem was solved to establish the Reynolds-number dependence of $\mathscr{E}$.

3.4. *The constraints on the I_k*

In this section, the boundary conditions (3.5) are used to derive expressions for the Reynolds number and the restriction on the slope, (3.9), in terms of the I_k and R_τ. An additional relation among the I_k is imposed by the third-derivative boundary conditions.

The second derivative of the mean is defined by

$$\pi^2 \frac{\mathrm{d}^2 U^+}{\mathrm{d}\phi^2} = \sin(\phi-\pi) \sum_0^{k_0} \sum_0^{k_0} I_k I_j \mathrm{e}^{\mathrm{i}(k-j)\phi}. \tag{3.14}$$

The I_k are real because I^*I is symmetric. Integration of (3.14), together with the first-derivative boundary conditions of (3.5), gives the first derivative of the mean,

$$\pi \frac{\mathrm{d}U^+}{\mathrm{d}\phi} = \sum_{k-j\neq -1} \frac{I_k I_j}{2\pi(k-j+1)} [\cos((k-j+1)\phi)-1] - \sum_{k-j\neq 1} \frac{I_k I_j}{2\pi(k-j-1)} [\cos((k-j-1)\phi)-1] + R_\tau. \tag{3.15}$$

From now on a single summation symbol will indicate summation over all indices from 0 to k_0 unless otherwise stated.

The mean velocity itself is determined by integration of (3.15), using the boundary condition $U^+ = -R/R_\tau$ at $\phi = 0$,

$$U^+ = -\frac{\phi}{\pi} + \sum_{k-j\neq -1} \frac{I_k I_j}{2\pi^2(k-j+1)} \left[\frac{\sin((k-j+1)\phi)}{(k-j+1)} - \phi\right] - \sum_{k-j\neq 1} \frac{I_k I_j}{2\pi^2(k-j-1)} \left[\frac{\sin((k-j-1)\phi)}{(k-j-1)} - \phi\right] + R_\tau \frac{\phi}{\pi}. \tag{3.16}$$

The condition $U^+ = R/R_\tau$ at $\phi = 2\pi$ must also be satisfied, the result being

$$R = R_\tau^2 - \frac{R_\tau}{2\pi} \sum_{k-j\neq -1} \frac{I_k I_j}{(k-j+1)} + \frac{R_\tau}{2\pi} \sum_{k-j\neq 1} \frac{I_k I_j}{(k-j-1)}. \tag{3.17}$$

Equation (3.17) is the Reynolds number in terms of the I_k (the mean velocity) and R_τ. It is one of three constraints on the I_k imposed in the optimization problem.

The slope restriction (3.9), needed to satisfy Fjørtoft's condition, is found from (3.15) at $\phi = \pi$,

$$R_\tau - \sum_{k-j\neq -1} \frac{I_k I_j}{2\pi} \frac{(1+(-1)^{k-j})}{(k-j+1)} + \sum_{k-j\neq 1} \frac{I_k I_j}{2\pi} \frac{(1+(-1)^{k-j})}{(k-j-1)} \geqslant 0. \tag{3.18}$$

Relation (3.18) is a second constraint on the I_k.

The only unused elements from the maximization problem in real space are the boundary conditions on the third derivative of the mean. Setting $\pi^2 \mathrm{d}^3 U^+/\mathrm{d}\phi^3 = 0$ at either boundary gives the third constraint on the I_k,

$$\sum_0^{k_0} I_k = 0. \tag{3.19}$$

Note that the boundary conditions on the second derivative of the mean are identically satisfied by the representation (3.14).

Once we express $\mathscr{E}$ in terms of I_k and R_τ, we will be ready to find its maximum constrained by the boundary conditions, a boundary layer of given scale, and inviscid stability in the interior. The problem is then to find the optimal R_τ and I_k spectrum at fixed R.

4. The optimal solution in Fejér space

4.1. *The Euler–Lagrange equations*

A search for the maximum of the efficiency function is motivated by the results of I. The efficiency function is the product of a drag coefficient, C_D, and the ratio of the fluctuation and mean dissipation rate integrals, I. The definitions of C_D and I are

$$C_D \equiv \frac{R_\tau^2}{R^2}, \quad I \equiv \frac{R_\tau \langle \beta \overline{uw}^+ \rangle}{\langle \beta^2 \rangle}, \tag{4.1}$$

where $\beta = -\mathrm{d}U^+/\mathrm{d}z$. Then

$$\mathscr{E} = \frac{R_\tau^3 \langle \beta \overline{uw}^+ \rangle}{R^2 \langle \beta^2 \rangle}. \tag{4.2}$$

Using the dissipation rate equation, (3.6), $\mathscr{E}$ may be written as

$$\mathscr{E} = \frac{R_\tau^2}{R\langle \beta^2 \rangle} - \frac{R_\tau^2}{R^2}. \tag{4.3}$$

An expression for $\langle \beta^2 \rangle$ is found by squaring (3.15) and averaging over the channel,

$$\langle \beta^2 \rangle = \left(\frac{R}{R_\tau}\right)^2 - \sum_{k-j\neq 1} \frac{I_k I_j I_m I_n \delta_{k-j-1,\,n-m+1}}{(2\pi)^2 (k-j-1)^2} + \sum_{k-j\neq -1} \frac{I_k I_j I_m I_n (2\delta_{k-j,\,n-m} - \delta_{k-j+1,\,n-m-1})}{(2\pi)^2 (k-j+1)^2}. \tag{4.4}$$

R_τ is expressed as a function of k_0 by (3.13).

To maximize $\mathscr{E}$ as a function of R_τ, for fixed R, one can first maximize $\mathscr{E}$ for fixed k_0 and fixed R. Then one must find the k_0 that corresponds to the absolute maximum of $\mathscr{E}$. There will be some error in the optimal value of the stress due to the discreteness of k_0. At Reynolds numbers of interest, however, k_0 is large enough to make this error negligible.

For fixed k_0 and fixed R, a maximum of $\mathscr{E}$ is a minimum of $\langle \beta^2 \rangle$ by (4.3). The Lagrangian for minimum $\langle \beta^2 \rangle$, subject to the boundary conditions, a boundary-layer scale of $4/k_0 = R_c^{\frac{1}{2}}/R_\tau$, and inviscid stability in the interior, is

$$\begin{aligned} L(R, k_0, b) = {} & \left(\frac{4R}{R_c^{\frac{1}{2}} k_0}\right)^2 - \sum_{k-j\neq 1} \frac{I_k I_j I_m I_n \delta_{k-j-1,\,n-m+1}}{(2\pi)^2 (k-j-1)^2} \\ & + \sum_{k-j\neq -1} \frac{I_k I_j I_m I_n (2\delta_{k-j,\,n-m} - \delta_{k-j+1,\,n-m-1})}{(2\pi)^2 (k-j+1)^2} + \lambda_1 \sum_0^{k_0} I_k \\ & + \lambda_2 \left[\frac{R_c^{\frac{1}{2}} k_0}{4} (1-b^2) - \sum_{k-j\neq -1} \frac{I_k I_j}{2\pi} \frac{(1+(-1)^{k-j})}{(k-j+1)} + \sum_{k-j\neq 1} \frac{I_k I_j}{2\pi} \frac{(1+(-1)^{k-j})}{(k-j-1)} \right] \\ & + \lambda_3 \left[R - \left(\frac{R_c^{\frac{1}{2}} k_0}{4}\right)^2 + \frac{R_c^{\frac{1}{2}} k_0}{8\pi} \sum_{k-j\neq -1} \frac{I_k I_j}{(k-j+1)} - \frac{R_c^{\frac{1}{2}} k_0}{8\pi} \sum_{k-j\neq 1} \frac{I_k I_j}{(k-j-1)} \right], \end{aligned} \tag{4.5}$$

where λ_1, λ_2 and λ_3 are Lagrange multipliers. The parameter b^2 is introduced to make the condition on the slope at the centreline, (3.18), an equality constraint. The critical boundary Reynolds number is the lower bound $R_c = 39.69$.

The Euler–Lagrange equations describing the extrema of $\mathscr{E}(R, k_0, b)$ result from variation of the Lagrangian (4.5). Variation with respect to the I_k gives

$$\sum_{k-j\neq -1} \frac{I_j I_m I_n(\delta_{k-j+1,n-m-1}-\delta_{k-j,n-m})}{\pi^2(k-j+1)^2} + \sum_{k-j\neq 1} \frac{I_j I_m I_n(\delta_{k-j-1,n-m+1}-\delta_{k-j,m-n})}{\pi^2(k-j-1)^2}$$
$$+\lambda_1 - \lambda_2\left[\sum_{k-j\neq -1} \frac{I_j(1+(-1)^{k-j})}{\pi(k-j+1)} - \sum_{k-j\neq 1} \frac{I_j(1+(-1)^{k-j})}{\pi(k-j-1)}\right]$$
$$+\lambda_3 \frac{R_c^{\frac{1}{3}} k_0}{4}\left[\sum_{k-j\neq -1} \frac{I_j}{\pi(k-j+1)} - \sum_{k-j\neq 1} \frac{I_j}{\pi(k-j-1)}\right] = 0, \tag{4.6}$$

where the summations are over all indices except k. Variation with respect to the Lagrange multipliers recovers the constraint equations (3.17), (3.18) and (3.19). The Euler–Lagrange equations are k_0+4 equations for $\{I_k : k = 0, 1, 2, \ldots, k_0\}$, λ_1, λ_2 and λ_3 in terms of R, k_0 and b. They are nonlinear, algebraic equations, solved using Newton's method.

The degree of this system can be reduced by a factor of two using the antisymmetry condition $I_k = -I_{k_0-k}$, which holds for the solution corresponding to the absolute maximum of $\mathscr{E}(R, k_0, b)$. (See §4.2.) The optimal b is found to be zero at all R. The optimal k_0 is a monotonically increasing function of R.

4.2. *The I_k spectra*

This section describes how selected information about the solutions of the Euler–Lagrange equations is used to track the absolute maximum of $\mathscr{E}(R)$.

There are k_0 relative maxima of the Euler–Lagrange equations (4.6) and (3.17)–(3.19). For the purpose of tracking the absolute maximum of $\mathscr{E}(R, k_0)$, we define $\{\mathscr{E}_n(R, k_0) : n = 1, 2, \ldots, k_0\}$ as the relative maxima. The subscript n denotes the relation of a maximum to its family, $\mathscr{E}_1(R, k_0)$ being the absolute maximum. It is also helpful to define $\mathscr{I}_n(k, R, k_0)$ to be the continuous analogue of the I_k spectrum corresponding to $\mathscr{E}_n(R, k_0)$. The negative of the I_k spectrum of $\mathscr{E}_n(R, k_0)$ is also a solution to the Euler–Lagrange equations with the same maximum and mean profile. This is an example of the non-uniqueness of the Fejér representation.

The I_k spectrum of $\mathscr{E}_1(R, k_0)$ satisfies the antisymmetry condition $I_k = -I_{k_0-k}$. The forms of the I_k spectra alternate between antisymmetric and symmetric with increasing n. The relative maximum $\mathscr{E}_n(R, k_0)$ is also characterized by the number of zeros of $\mathscr{I}_n(k, R, k_0)$. The number of zeros in $\mathscr{I}_n(k, R, k_0)$ is n. For example, $\mathscr{I}_1(k, R, k_0)$ has one zero at $k = \frac{1}{2}k_0$.

To find the maximum $\mathscr{E}(R)$, we first solve the Euler–Lagrange equations for $\mathscr{E}_1(R, k_0)$ and then optimize over k_0. At each k_0, we need only look for the I_k spectrum that is antisymmetric, with one zero at $k = \frac{1}{2}k_0$ in $\mathscr{I}_1(k, R, k_0)$.

The spectra of maximum $\mathscr{E}(R)$ consist of two sets of points that look roughly like points from two sine functions. The I_k spectrum for $\mathscr{E}(700)$ is shown in figure 1 ($k_0 = 93$ is the optimal value of k_0 for $R = 700$). Unfortunately, no satisfactory approximation in terms of sine functions was found that preserves all the characteristics of the maximum-$\mathscr{E}$ mean.

At a given R, the distance between the sets, together with the magnitude of I_{k_0}, determines the size of the interior of the mean velocity. The larger they are, the

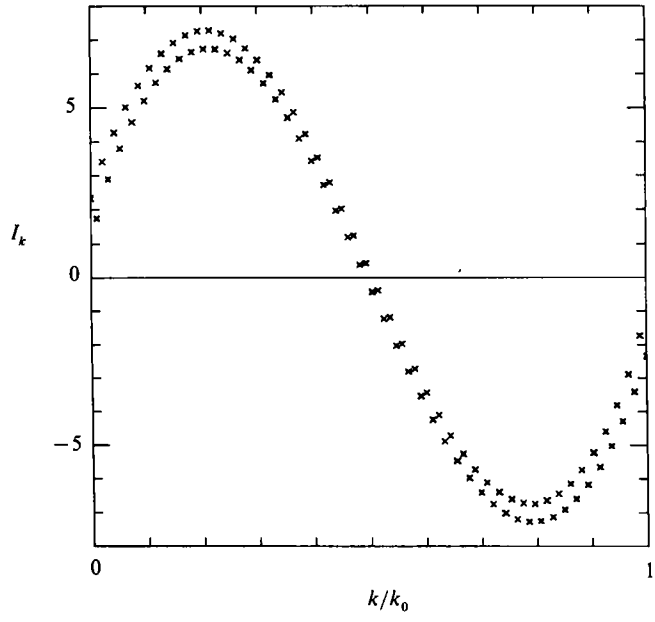

FIGURE 1. The I_k spectrum for the absolute maximum of $\mathscr{E}$ at $R = 700$ ($k_0 = 93$).

bigger the interior of the mean profile. These two features are equivalent to the size of the jumps at the ends of the I_k spectra for optimal Poiseuille flows (see I).

5. The mean flow of maximum efficiency $\mathscr{E}$

5.1. *The optimal profile*

The mean flow associated with maximum $\mathscr{E}$ is shown in figure 2 as a function of Reynolds number, where $V^+ \equiv U^+_{\mathrm{MAX}} + U^+$. Based on $R_c = 39.69$, the Reynolds numbers of the profiles in figure 2 increase from 100 to 1600 in increments of 100. In figures 2 and 3, an arrow indicates the direction of increasing Reynolds number. An obvious feature is the extended linear region on the semi-log plot, which develops after an initial transition period. There is a *slight* downward drift of the log layer as the Reynolds number increases. This Reynolds-number dependence is no more than, and perhaps consistent with, the observations. For all practical purposes, the slopes of both the maximum-$\mathscr{E}$ flow and realized turbulent Couette flow are constant. For the maximum $\mathscr{E}$ with $R_c = 39.69$, the value of the log slope is close to 1.0 and the intercept is approximately 2.4.

The other striking feature is the decreasing interior. First there is an initial range of R in which the profile seems to be approaching a stable form. The interior is decreasing in this stage, which is up to $R = 400$. Although not emphasized here, the upper-bound theory gives a detailed prediction for the evolution of the mean in the transition region between laminar flow and fully developed turbulence.

Following the transition period, the interior stays constant over intervals of Reynolds number before decreasing in discrete steps. Each higher Reynolds-number range is longer than the last. The length of the interval is a constant factor, δ_{R_c}, multiplied by $(p+2)$, where p numbers the stable interior forms. For $R_c = 39.69$, the value of δ_{R_c} is 100. The first stable form appears at $R = 400$. The next stable interior forms are first seen at $R = 700$, 1100 and 1600, corresponding to $p = 2$, 3 and 4. The

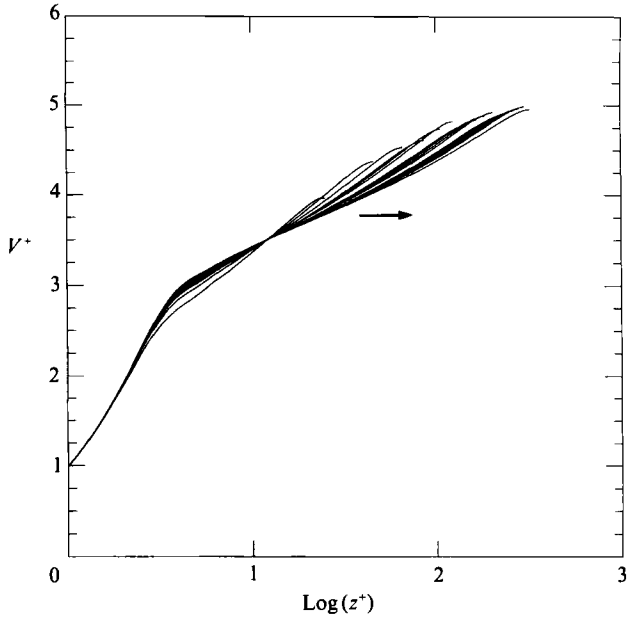

FIGURE 2. The maximum-$\mathscr{E}$ profiles from transitional to fully developed flow. Based on $R_c = 39.69$, R increases from 100 to 1600 in increments of 100. The values of k_0 are 16, 29, 42, 55, 67, 79, 93, 105, 117, 129, 143, 155, 167, 179, 191 and 205, respectively.

first interval of R is $3\delta_{R_c}$, the second $4\delta_{R_c}$ and the third $5\delta_{R_c}$. An ordered, discrete convergence is suggested. Unfortunately we did not have the computational power to explore higher Reynolds numbers. However, we have reached Reynolds numbers near 30000 based on an experimental R_c (see §5.3).

A velocity defect plot (figure 3) quantifies the behaviour of the interior. The values at 0.75 of the half-channel width for the first four stable interior forms (based on the average) are 0.827, 0.765, 0.720 and 0.683. The increments are 0.062, 0.045 and 0.037 and are decreasing. A decreasing interior and a logarithmic law together imply that the logarithmic layer is a smaller percentage of the (unscaled) flow with increasing Reynolds number.

Also notable is the fact that the slope of the mean decreases to zero at the centreline of the channel. The consistency (or inconsistency) of the zero slope with the data is addressed in §5.3.

5.2. *Comparison with the maximum-$\mathscr{E}$ Poiseuille flow*

It is informative to compare, at fixed R_c, the maximum-$\mathscr{E}$ mean profiles for Couette and Poiseuille flows (see I). The boundary regions of both flows are dominated by the strong shear at the wall and are almost identical. However, the logarithmic slope for Couette flow is only 70% of that for Poiseuille flow. The log slope is observed to be roughly the same in realized turbulent Couette and Poiseuille flows. One anticipates that a larger R_c will be necessary for the maximum-$\mathscr{E}$ flow to approach the data than was found for Poiseuille flow.

Section 5.3 shows that for Couette flow a realistic estimate is $R_c \approx 800$, while for Poiseuille flow $R_c \approx 480$ was found in I. The heights corresponding to a smallest roll are approximately $z^+ = 13.5$ for Couette flow and $z^+ = 11$ for Poiseuille flow.

The interior regions of the maximum-$\mathscr{E}$ Couette and Poiseuille profiles are quite

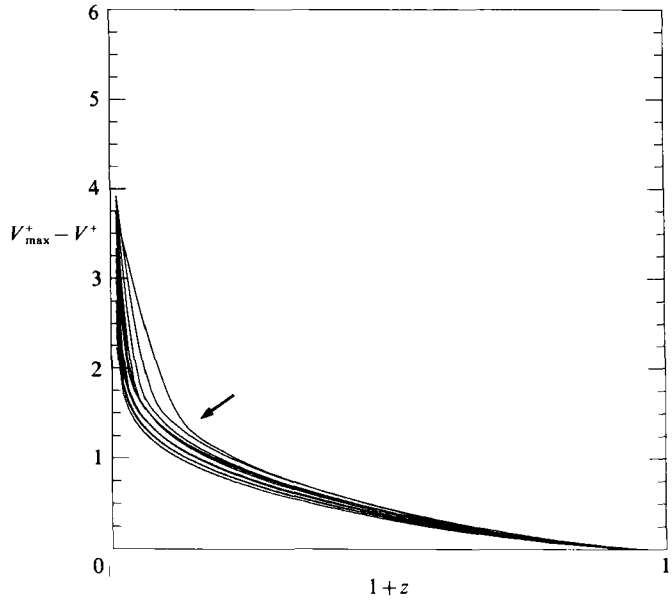

FIGURE 3. The velocity defect of the maximum-$\mathscr{E}$ flow decreases in steps. The steps are smaller with increasing R suggesting an ordered, discrete convergence as $R \to \infty$. The values of R and k_0 are as in figure 2.

different. A velocity defect *law* is found for Poiseuille flow. That is, the velocity defect is quickly asymptotic. The difference is consistent with the physics of the two flows. Their opposing symmetries provide a contrast in behaviour, on average, in the centre. In Couette flow, the mean shear and correlation coefficient, $-\overline{uw}/\langle u_{\rm rms} w_{\rm rms}\rangle$, are observed to be almost uniform in the central 40% of the channel. Therefore so are quantities such as $R_\tau^3 \beta \overline{uw}$ and $R_\tau^2 \beta^2$. In Poiseuille flow, all of these quantities go rapidly to zero in the central region.

5.3. *Quantitative comparison with the data*

If maximum $\mathscr{E}$ is approached by the fluid, the upper bound mean flows provide testible predictions, such as continued decrease of the velocity defect. The purpose of this section is a critical assessment of maximum $\mathscr{E}$ as a statistical stability criterion in Couette flow.

All available data for turbulent Couette flow is restricted to $R < 20000$ (based on the half-channel width and half of the maximum relative velocity). A recent study by El Telbany & Reynolds (1982) determined a logarithmic slope of 5.87 and an intercept of 5.2 (figure 5). These values are significantly different from those established by earlier experimenters. Robertson & Johnson (1970) found 5.6 and 5.6, and Reichardt (1959) gave 5.75 for the slope and 5.5 for the intercept. The earlier values are essentially the same as in Poiseuille flow. We use the data recorded by El Telbany & Reynolds because it is more recent, and because it is presented in velocity defect form. Their velocity defect data, reproduced in figure 4, are the most important evidence in support of the maximum-$\mathscr{E}$ hypothesis.

The observed velocity defect is decreasing, apparently in increments similar to the maximum-$\mathscr{E}$ flow. The velocity defects at 0.75 of the half-channel width are about 4.9 at $R = 9500$, 4.1 at $R = 12640$ and 14250 and 3.8 at $R = 18960$. From only four data points, a pattern to the decrease is only speculative.

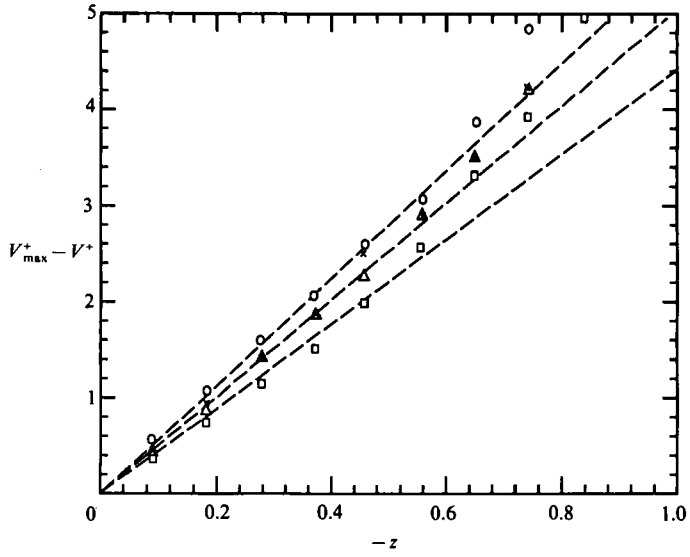

FIGURE 4. The observed velocity defect: ○, $R = 9500$; △, $R = 12640$; ×, $R = 14250$; □, $R = 18960$. Reproduced from El Telbany & Reynolds (1982).

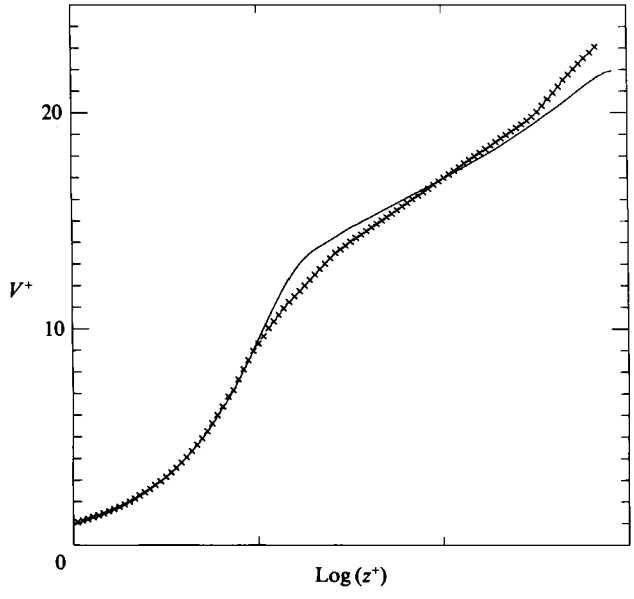

FIGURE 5. The maximum-$\mathscr{E}$ flow numerically determined using $R_c = 800$ (solid line) and the data of El Telbany & Reynolds (1982) (×), both at $R = 18000$.

A quantitative comparison with the data is made using a value for R_c with which the optimal mean approaches the data. One must be careful that this 'experimental' value of R_c still provides an upper bound on $\mathscr{E}$. Figure 5 displays the data and the maximum-$\mathscr{E}$ flow numerically calculated using $R_c = 800$ ($k_0 = 117$). The Reynolds numbers of both are about 18000. The slope of the theoretical curve is 5.8 and its intercept is 7.6. As in Poiseuille flow, the experimental profile has a more gradual transition from laminar boundary layer to logarithmic sublayer, a higher slope and a larger interior.

For $R_c = 800$, the value $\delta_{R_c} = 2015$ defines the ordered sequence of transitions in the mean profile. The first interval of stable interior begins at $R = 10075$ and has length $3\delta_{R_c}$. The second and third stable forms appear at $R = 16120$ and $R = 24180$, and persist for $4\delta_{R_c}$ and $5\delta_{R_c}$, respectively. The highest Reynolds number achieved is $R = 32250$ and marks the beginning of a fourth region of stable interior form. The theoretical velocity defects were recalculated using $R_c = 800$. As expected from figure 5, they are low compared to the data. The velocity defects at 0.75 of the half-channel width are 3.71, 3.43, 3.23 and 3.07, respectively, in the four regions. Further decrease in the realized velocity defect is predicted, at least up to $R = 30000$.

Finally the issue of the local slope at the centre must be addressed. All of the experimenters to date have reported a finite slope at the centreline. Reichardt's data are plotted to suggest a normalized slope of 0.25 at $R = 1450$ and 0.20 at $R = 17000$. The normalization is with respect to the maximum velocity. His data points, however, are quite far from the centreline.

El Telbany & Reynolds also report a finite slope at the centreline, but it is decreasing with increasing R (figure 5). Their values of the normalized slope are 0.26 at $R = 9500$, 0.23 at $R = 12640$, 0.22 at $R = 14250$ and 0.19 at $R = 18960$. These values are consistent with Reichardt's. Their data points are closer to the centre and therefore more convincing. The local slope at the centreline may decrease to zero at high enough Reynolds number, which would perhaps indicate that maximum $\mathscr{E}$ is an asymptotic state.

What is most significant is the *global* behaviour of the interior flow: both the experiments and the maximum-$\mathscr{E}$ flow suggest decreasing shear in a finite central region as the Reynolds number increases. Numerical calculations at low Reynolds numbers also show a decreasing interior shear with Reynolds number (Lee 1989). Thus there is evidence that realized turbulent Couette flow moves closer to a state of maximum-$\mathscr{E}$ as R increases.

5.4. *Adjacent integrals with non-zero slope at the centre*

Among moments of the class $\{R_\tau^{2n} I(R) : n \geqslant 0\}$ ($\mathscr{E}$ corresponds to $n = 1$), there is none whose maximization leads to a logarithmic law, a decreasing velocity defect for $R < 18000$, and a finite slope at the centreline.

An exponent greater than 2 results in a more flat-topped profile with a more rapidly vanishing velocity defect. All exponents greater than 2 result in zero slope at the centre.

An exponent less than 2 yields a more linear profile. As n decreases, the curvature of the mean near the centre decreases until it is linear with finite slope. However, for all n which lead to a finite slope through the centre, the velocity defect is increasing. In fact, even for $n = \frac{3}{4}$, which still exhibits a curved inflexion point at the centre, the velocity defect is increasing.

The observed velocity defect may not continue to decrease, but it probably does not begin to *increase*. Among the maxima of $\{R_\tau^{2n} I(R), n \geqslant 0\}$, even a constant velocity defect is associated with a zero local slope at the centre.

5.5. *Discussion*

There is some disagreement with respect to Reichardt's (1959) data. Busse suggests that Reichardt's data is asymptoting to $\frac{1}{4}$ of the shear of the laminar solution (Busse 1970). Busse's maximum transport solution exhibits a '$\frac{1}{4}$'-law outside the viscous boundary layer. However, we estimate, from the same data, that the interior shear is already about $\frac{1}{4}$ of its laminar value at $R = 1450$. The shear appears to be about $\frac{1}{5}$

of its laminar value at $R = 17000$, the highest Reynolds number achieved in Reichardt's study. The data of El Telbany & Reynolds also shows a shear smaller than $\frac{1}{4}$ of the laminar value for Reynolds numbers above 10000.

All other evidence is against maximum transport as a statistical stability criterion for shear flows. Using the present formalism, the maximum transport means are 'flat-topped' for both Poiseuille and Couette flows; there is no log law or velocity defect law in either flow. Neither are log or velocity defect laws found from Busse's formalism (Busse 1970; I). The fact that the maximum transport solutions do not exhibit the well-established laws of Poiseuille flow sheds doubt on their relevance to Couette flow. It is unlikely that the two flows are governed by different principles.

On the other hand, we find that maximum $\mathscr{E}$ predicts both a log law and a velocity defect law in Poiseuille flow, and a log law in Couette flow. The decreasing velocity defect of maximum $\mathscr{E}$ in Couette flow would seem at first to question its generality as a statistical stability criterion for shear flows. However, the data of El Telbany & Reynolds shows a decreasing velocity defect and a decreasing slope through the centreline for R as high as 18000. The zero slope through the centreline of maximum $\mathscr{E}$ is not observed at low R, but may be approached at high R. Experiments at high Reynolds numbers are needed to establish the asymptotic behaviour of turbulent Couette flow and thereby to determine the limitations of maximum $\mathscr{E}$.

6. Conclusions and prospects

An upper bound of the efficiency function, $\mathscr{E}$, gives the correct scaling laws in turbulent Poiseuille flow. The maximum-$\mathscr{E}$ flow exhibits both a logarithmic law and a velocity defect law. The success of maximum $\mathscr{E}$ to qualitatively describe turbulent Poiseuille flow suggests an investigation of its generality.

Couette flow is thought of as the simplest example of the shear mechanism. Unfortunately, because experiments are difficult, the data on turbulent Couette flow are scarce and restricted to $R < 20000$. All available data exhibit a logarithmic law, though the value of the slope varies with experiment. The presumption has been that there is also a velocity defect law in turbulent Couette flow. The data of El Telbany & Reynolds, however, show a decreasing velocity defect and a decreasing slope at the centreline. That the two flows scale differently in the interior is consistent with the constraints imposed by their symmetries.

Maximum $\mathscr{E}$ in Couette flow predicts a logarithmic law, a decreasing velocity defect and a slope of zero at the centreline. High-Reynolds-number experiments and/or numerical data are needed to convincingly establish the behaviour of the velocity defect in Couette flow. They will strengthen or weaken the hypothesis that maximum $\mathscr{E}$ is a statistical stability criterion for both Couette and Poiseuille flows.

It is possible that maximum $\mathscr{E}$ is generalizable to other kinds of turbulence as well. For example, maximum transport and maximum $\mathscr{E}$ may lead to the same results for thermal convection at high Rayleigh numbers, Ra. For fixed Ra, maximum transport is equivalent to maximum stress, R_τ^2, while maximum $\mathscr{E}$ is equivalent to maximum $R_\tau^2 I$. Owing to the different inviscid stability conditions for shear and convective flows, it is plausible that I is asymptotically approaching a constant in convection whereas it is growing logarithmically in shear flow.

Turbulent flows driven by both shear and buoyancy-like forces are of interest to a large audience. They have meteorological, geophysical and engineering importance. They also have a 'simple' laboratory example: Taylor–Couette flow between rotating cylinders. In the case of a narrow gap between the cylinders, the flow

approaches flow between parallel plates. If the outer cylinder rotates faster than the inner cylinder, the flow is centrifugally stabilized. In the reverse situation the flow is centrifugally destabilized. In unstable Taylor–Couette flow, at high enough Reynolds numbers, both shear and centrifugal forces are comparable.

Nickerson (1969) considered low-Reynolds-number, centrifugally unstable Taylor–Couette flow. He found that maximum stress is an adequate first description of the physics. Again one might ask if the results of maximum $\mathscr{E}$ would be significantly different.

The data for high-Reynolds-number Taylor–Couette flow present another challenge to the hypothesis that maximum $\mathscr{E}$ is a general statistical stability criterion. Although Smith & Townsend (1982) state that they find a von Kármán logarithmic slope, their graphs indicate otherwise. The slope appears close to 1.5, not 2.44 (base e). Although our predictions are as yet qualitative, the maximum-$\mathscr{E}$ flow may be indicative.

The methods here may not be directly applicable to more complicated turbulent flows, but it is clear that simplified upper-bound schemes can be constructed. Flow quantities can then be isolated whose upper bounds reflect the average properties of the turbulence. Studies of flows such as Taylor–Couette flow will improve our techniques, force a better understanding of the stability processes, and determine the limitations of maximum $\mathscr{E}$.

Given an upper-bound flow that is qualitatively like an observed turbulent flow, quantitative difference can be removed with more constraints. In parallel shear flows, the vorticity dissipation rate integral alters the downstream-roll structure predicted by the energy dissipation rate integral (I; Malkus 1968). Such a mechanistic change will probably be accompanied by a significant quantitative improvement. Finally, disorder and time dependence can be introduced with a perturbative analysis of the upper-bound solutions (I). Upper-bound theory is thus a step towards a satisfactory and completely deductive description of shear turbulence and, we hope, of more complicated kinds of turbulence as well.

I am deeply indebted to Professor W. V. R. Malkus for the teaching and guidance he provided through the completion of this work. I am grateful to Fabian Waleffe for his advice with respect to the numerics involved, and for helpful comments on several drafts of this work. Finally, I would like to thank the referees for their very valuable reviews of the manuscript. This work was supported by the National Science Foundation under grant ATM86-11727. The computations were done on the Sun system of the MIT Mathematics department.

REFERENCES

Arnol'd, V. I. 1965 Conditions for nonlinear stability of stationary plane curvilinear flows of an ideal fluid. *Dokl. Akad. Nauk SSSR* **162**, 975.

Bayly, B. J., Orszag, S. A. & Herbert, T. 1988 Instability mechanisms in shear-flow transition. *Ann. Rev. Fluid Mech.* **20**, 359.

Busse, F. H. 1969*a* Bounds on the transport of mass and momentum by turbulent flow between parallel plates. *Z. Angew. Math. Phys.* **20**, 1.

Busse, F. H. 1969*b* On Howard's upper bound for heat transport by turbulent convection. *J. Fluid Mech.* **37**, 457.

Busse, F. H. 1970 Bounds for turbulent shear flows. *J. Fluid Mech.* **41**, 219.

Busse, F. H. 1978 The optimum theory of turbulence. *Adv. Appl. Mech.* **18**, 77.

Drazin, P. G. & Reid, W. H. 1981 *Hydrodynamic Stability*. Cambridge University Press.

EL TELBANY, M. M. M. & REYNOLDS, A. J. 1982 The structure of turbulent plane Couette flow. *Trans. ASME* I: *J. Fluids Engng* **104**, 367.

HOWARD, L. N. 1972 Bounds on flow quantities. *Ann. Rev. Fluid Mech.* **4**, 473.

JOSEPH, D. D. 1976 *Stability of Fluid Motions*, Vols. 1 and 2. Springer.

LEE, M. J. 1989 *CTR Annual Research Briefs.* Center for Turbulence Research, Stanford University.

MALKUS, W. V. R. 1954 The heat transport and spectrum of thermal turbulence. *Proc. Roy. Soc. Lond.* A **225**, 196.

MALKUS, W. V. R. 1956 Outline of a theory of turbulent shear flow. *J. Fluid Mech.* **1**, 521.

MALKUS, W. V. R. 1968 A proof of the non-existence of steady two dimensional disturbances in unbounded plane parallel flows (unpublished).

MALKUS, W. V. R. 1979 Turbulent velocity profiles from stability criteria. *J. Fluid Mech.* **90**, 401.

MALKUS, W. V. R. & SMITH, L. M. 1989 Upper bounds on functions of the dissipation rate in turbulent shear flow. *J. Fluid Mech.* **208**, 479 (referred to herein as I).

NICKERSON, E. C. 1969 Upper bounds on the torque in cylindrical Couette flow. *J. Fluid Mech.* **38**, 807.

REICHARDT, H. 1959 Gesetzmässigkeiten der geradlinigen turbulenten Couetteströmung. *Mitt. Max Planck Inst. Strömungsforschung, Göttingen* **22**, 45.

ROBERTSON, J. M. & JOHNSON, H. F. 1970 Turbulence structure in plane Couette flow. *J. Engng Mech. Div. ASCE* **96**, 1171.

SMITH, G. P. & TOWNSEND, A. A. 1982 Turbulent Couette flow between concentric cylinders at large Taylor numbers. *J. Fluid Mech.* **123**, 187.